Recursive Least Squares and Adaptive Kalman Filter-Based State and Parameter Estimation for Series Arc Fault Detection on DC Microgrids

Kaushik Gajula, *Graduate Student Member, IEEE*, Lalit Kishore Marepalli, *Graduate Student Member, IEEE*, Xiu Yao, *Member, IEEE*, and Luis Herrera, *Member, IEEE*

***Abstract*— In this article, we present a recursive least squares (RLS) and adaptive Kalman filter (AKF)-based state and parameter estimation (SE and PE) for series arc fault (SAF) detection and identification on dc microgrids. It is evident from the state-of-the-art research on dc SAFs that due to the lack of zero crossings and low current of the fault, the detection/identification of a SAF is difficult. Furthermore, due to the unplanned placement of sensors and the effect of SAF's noise signatures on the adjacent sensors, we present a RLS-based SE for voltages and injection currents. The injection currents and nodal voltages from the states are then used by the AKF for a quick SAF detection, by estimating line admittances on the microgrid. The simulation results, control hardware in loop (CHIL), and experimental results are presented to manifest the SE–PE technique's potential.**

***Index Terms*— Adaptive Kalman filter (AKF), dc microgrid, fault detection, fault identification, parameter estimation (PE), recursive least squares (RLS), series arc fault (SAF), state estimation (SE).**

I. Introduction

THE series arc fault (SAF) is one of the primary challenges that hinder a full-scale deployment of dc microgrids. In accordance with the rise in demand of renewable energy as a power source and a consistent choice of loads being dc, it is easier to deploy the microgrids/buses in dc. As most sources and loads require a dc stage, dc microgrids can also help in reducing the number of power conversion stages compared to ac networks [1], [2]. Furthermore, the power losses in dc transmission are lesser in comparison to an ac transmission. On this premise, a dc microgrid is an apt choice for modern microgrid deployment and it is necessary to find solutions to challenges like the SAF. The SAF is a consequence of line breakage which is caused by wear and tear or loosely connected wires. The SAF further induces noise in the circuit due to an ionized air gap that forms between the two conductors which have a high relative charge [3]–[5]. The low-current characteristic feature of a SAF makes detecting and identifying it far more difficult than parallel/ground faults.

Manuscript received 20 July 2021; revised 5 November 2021; accepted 8 December 2021. Date of publication 13 December 2021; date of current version 2 August 2022. This work was supported by the National Science Foundation (NSF) under Award 1855888 and Award 1809839. Recommended for publication by Associate Editor Jon Are Suul. *(Corresponding author: Kaushik Gajula.)*

The authors are with the Department of Electrical Engineering, University at Buffalo, Buffalo, NY 14260 USA (e-mail: kaushikk@buffalo.edu).

Color versions of one or more figures in this article are available at https://doi.org/10.1109/JESTPE.2021.3135409.

Digital Object Identifier 10.1109/JESTPE.2021.3135409

In recent years, the state-of-the-art research in SAF detection/identification includes frequency- and time domain-based approaches. Fourier transform [6], [7] and wavelet decomposition [4], [8] are few of the common procedures that constitute the frequency domain-based analysis for SAF detection. In [9], a method of SAF detection is presented for the load side power electronics, based on the electrode-dependent initial voltage drop that occurs at the arc initiation. While the detection of a SAF is achievable, identifying the faulted line is difficult using frequency domain-based approaches since the arc noise propagates to the adjacent lines in the network. Typical time domain-based approaches include parameter estimation (PE)/state estimation (SE) algorithms like least squares (LS), Kalman filter (KF) and their variants, and other convex minimization algorithms. Fault detection and identification on a distribution node using gradient algorithm is shown in [10]. Recursive LS (RLS) and KF are used for detecting a SAF and identifying the faulted line on a distribution node in [11]. Detection and identification of SAF on a dc microgrid using KF and adaptive-KF (AKF) is presented in [12]. A SAF detection algorithm is proposed in [13] which analyzes line current drops, line current average value change rates, the standard deviations of the line current, and the ac component of the supply voltage. A time domain technique based on the mathematical morphology called the decomposed open-close alternating sequence (DOCAS) is proposed in [14] for SAF detection and identification on a typical PV system.

Application of ensemble machine learning algorithm for SAF detection is presented in [15] and [16]. The algorithm is trained with experimental arc fault data, and an adaptive normalization function is designed to mitigate false positive classification caused by load changes. A domain adaptation combined with deep convolutional generative adversarial network (DA-DCGAN) approach for SAF detection on a PV circuit is presented in [17]. A dual state and PE is proposed in [18], where the SE is performed using LS algorithm. In this approach of SE, the measurement samples are collected over a period of time and the cost function is formulated over a window to provide real-time state estimates. However, this causes a delay in the detection of SAF and identification of the faulted line due to the time consumed in collecting the samples. Furthermore, the LS-based SE requires the calculation of a large matrix inverse, making this approach computationally expensive. Using RLS method presented in

this article, we can estimate the states at every iteration making the execution and fault detection much faster.

Recently, SE for distribution grids has gained popularity in an effort to keep the microgrid under control, because of frequent fault scenarios and cyber-attacks/bad data injections. A two-step method to identify topology, estimate line parameters, and recover missing voltage angles in common, is proposed in [19]. The algorithm was further tested on an IEEE 33 and IEEE 123 bus systems. The step 1 of the algorithm includes basic identification, obtain basic topology and line parameters through linear regression, while step 2 corrects them by a specialized Newton–Raphson method. In [20], the error in-variables model in a maximum-likelihood estimation framework for joint line parameter and topology estimation in distribution grids is proposed. A novel maximum likelihood blind estimation of states and topology (ML-BEST) method for power systems by formulating the problem as graph blind source separation with a Laplacian mixing matrix is proposed in [21]. In addition to estimation of the topology and event detection, Ardakanian *et al.* [22] presents a linear regression form of the nodal equation to estimate the line admittances.

Our contributions in this article include, a faster dual SE and PE in comparison to [18], where the objective is to evaluate the line admittance of a dc microgrid when every node does not contain all the measurement sensors. The RLS technique using a sparse tableau analysis (STA) [23], [24] is presented for SE at every iteration, when measurements are obtained. The nodal currents and voltages from the SE are forwarded to the AKF for PE, which provides real-time line admittance values for all the lines in a microgrid. When a line admittance shows a significant drop in its value, the SAF is instantaneously detected and the faulted line is identified.

This article is structured as follows. In Section II, the SE by RLS is explained and in Section III, PE by AKF is discussed. In Section IV, case studies and simulation results are presented and in Section V, control hardware in loop (CHIL) result is demonstrated. Experimental result obtained from a small microgrid test-bed is shown in Section VI and finally, conclusion and future work are stated in Section VII.

We use the following notations in this article. For a matrix $A \in \mathbb{R}^{m\times n}$, its vectorization is denoted as $\text{vec}(A) = (A_{11}, \ldots, A_{m1}, A_{12}, \ldots, A_{m2}, \ldots, A_{1n}, \ldots, A_{mn})^T$. An identity matrix is denoted by $\mathcal{I}$. For a set $\mathcal{X}$, its cardinality (number of elements) is denoted by $|\mathcal{X}|$. A column vector of ones of length m is written as $\mathbf{1}_m$. The notation $\|x\|_J^2$ denotes $x^T Jx$. The symbol $\otimes$ is used to define the Kronecker product.

II. State Estimation

In this section, we describe a typical dc microgrid with respect to its states and present the RLS algorithm for estimating them when a reduced number of sensors are used.

A. Microgrid Description for SE

A dc microgrid can be defined by a directed graph

$$\mathcal{G} = (\bar{\mathcal{V}}, \mathcal{E}) \tag{1}$$

where $\bar{\mathcal{V}}$ and $\mathcal{E}$ represent the set of nodes and edges, respectively. The nodes are of the form $\bar{\mathcal{V}} = \{0, 1, \ldots, N\}$, where 0 is defined as the ground or reference node. The total number of nodes are given by $|\bar{\mathcal{V}}| = N + 1$ and the number of edges are $|\mathcal{E}| = E$. A reduced set of nodes can then be defined as $\mathcal{V} = \bar{\mathcal{V}} - \{0\}$ (i.e., excluding the ground node) with $|\mathcal{V}| = N$. The set of edges $\mathcal{E} \subseteq \bar{\mathcal{V}} \times \bar{\mathcal{V}}$ will be defined as follows $\mathcal{E} = \{(p, 0_g), \ldots, (q, 0_L), \ldots, (i, j), \ldots\}$ where (i, j) implies current direction from node $i \in \bar{\mathcal{V}}$ to node $j \in \bar{\mathcal{V}}$, the edge $(p, 0_g)$ implies a generator is connected to node $p \in \mathcal{V}$, and $(q, 0_L)$ implies a load is connected to node $q \in \mathcal{V}$.

The STA analysis will be used to formulate the Kirchhoff current/voltage laws (KCL and KVL) and the branch equations which govern the behavior of the microgrid defined by $\mathcal{G}$. The STA can be used to include a larger variety of sensors (e.g., line current, generation current, load currents, etc.) and components (e.g., nonlinear elements) which may not be explicitly defined using the more traditional nodal analysis [24].

The set of line currents will be defined by $l \in \mathbb{R}^E$, the branch voltages as $e \in \mathbb{R}^E$, and the node voltages as $V \in \mathbb{R}^N$. These vectors are of the following form:

$$\begin{aligned} l &= \begin{pmatrix} I_{p0_g} & \cdots & I_{q0_L} & \cdots & I_{ij} & \cdots \end{pmatrix}^T \\ e &= \begin{pmatrix} V_{p0_g} & \cdots & V_{q0_L} & \cdots & V_{ij} & \cdots \end{pmatrix}^T \\ V &= \begin{pmatrix} V_1 & \cdots & V_N \end{pmatrix}^T \end{aligned} \tag{2}$$

written in the same order as $\mathcal{E}$ and $\mathcal{V}$. The reduced oriented incidence matrix, $\mathcal{A} \in \mathbb{R}^{N\times E}$, can then be used to derive the KCL and KVL equations. The matrix $\mathcal{A}$ associates each node/bus with its incident edges/lines. For example, for a line $(i, j) \in \mathcal{E}$, the i^{th} row of $\mathcal{A}$ will have a "1" in the column related to this edge and a "-1" in the j^{th} row.

The STA [23]–[25] is then composed of

$$\mathcal{A}l = 0, \quad \text{(KCL)} \tag{3}$$

$$\mathcal{A}^T V = e, \quad \text{(KVL)} \tag{4}$$

and the branch equations

$$\hat{Y}_{ij} V_{ij} - I_{ij} = 0 \quad \forall (i, j) \in \mathcal{E},\ i, j \in \mathcal{V} \tag{5}$$

which can be written in matrix form as

$$K_e(\hat{\Upsilon})e + K_l l = 0. \tag{6}$$

The dimension of matrices K_e and K_l is $E_{\text{in}} \times E$, where $E_{\text{in}} \leq E$ is the number of lines (excluding generator and loads) in the network. The vector $\hat{\Upsilon} \in \mathbb{R}^{E_{\text{in}}}$ consists of the line admittances Y_{ij} (to be estimated by AKF). The matrix $K_e(\hat{\Upsilon})$ is then updated after every update of the PE iteration.

The states of the dc microgrid are then defined as

$$x = \begin{pmatrix} e^T & V^T & l^T \end{pmatrix}^T \tag{7}$$

and (3), (4), and (6) can be written as

$$\underbrace{\begin{pmatrix} 0 & 0 & \mathcal{A} \\ \mathcal{I} & -\mathcal{A}^T & 0 \\ K_e & 0 & K_l \end{pmatrix}}_{T} \underbrace{\begin{pmatrix} e \\ V \\ l \end{pmatrix}}_{x} = \begin{pmatrix} 0 \\ 0 \\ 0 \end{pmatrix}, \quad (Tx = 0). \tag{8}$$

The voltage and line current measurements are stored in the vector y and the estimate of the state vector represented by $\hat{x}(k)$ is updated by RLS at every iteration k. The linear regression form relating the output vector to the microgrid's state vector is given by

$$\underbrace{\begin{pmatrix} V_{\text{meas}}^T & I_{\text{meas}}^T \end{pmatrix}^T}_{y} = C \underbrace{\begin{pmatrix} \hat{e}_i^T & \hat{V}_j^T & \hat{I}_j^T \end{pmatrix}^T}_{\hat{x}}. \tag{9}$$

B. Recursive Least Squares-Based SE

Using (8) and (9), a quadratic optimization problem can be formulated as follows [18]:

$$\min_{\hat{x}} \ \frac{1}{2}\|y - C\hat{x}\|_J^2 + \frac{1}{2}\|T\hat{x}\|_D^2 \tag{10}$$

where matrices J and D are positive definite matrices used as weights. Rather than solving (10) at every iteration or after a collection of samples, we consider a recursive approach to obtain faster estimates. For this purpose, we can combine (8) and (9) as follows:

$$\tilde{y}(k) = \tilde{C}\hat{x}(k) + v_{\text{se}}(k) \tag{11}$$

where

$$\tilde{y} = \begin{pmatrix} y \\ 0_{(\text{rows}(T),1)} \end{pmatrix}, \quad \tilde{C} = \begin{pmatrix} C \\ T \end{pmatrix} \tag{12}$$

and $v_{\text{se}}(k) \sim \mathcal{N}(0, R_{\text{se}}(k))$ is the measurement noise at time k.

Using the RLS algorithm, the state estimate $\hat{x}(k)$ is updated at every kth interval of time by

$$\hat{x}(k) \ = \hat{x}(k-1) + K_{\text{se}}(k) \ [y(k) \ - \tilde{C}(k) \ \hat{x}(k-1)]. \tag{13}$$

Defining the error as $\hat{x}(k) - x$, its covariance matrix is denoted by $P_{\text{se}}(k)$

$$P_{\text{se}}(k) = E[(\hat{x}(k) - x)(\hat{x}(k) - x)^T] \tag{14}$$

with initial condition $P_{\text{se}}(0) = m\mathcal{P}_{\text{se}}$. The matrix $\mathcal{P}_{\text{se}}$ is an identity matrix of appropriate dimension. We calculate $P_{\text{se}}(k)$ at every k^{th} instant as

$$P_{\text{se}}(k) \ = \frac{1}{\lambda}\,[P_{\text{se}}(k-1) - K_{\text{se}}(k)\tilde{C}(k)P_{\text{se}}(k-1)]. \tag{15}$$

The gain used to minimize error between the state and its estimate is given by

$$K_{\text{se}}(k) \ = P_{\text{se}}(k-1)\tilde{C}^T(k) \ [\tilde{C}(k) \ P_{\text{se}}(k-1)\tilde{C}^T(k) \ + \lambda R_{\text{se}}]^{-1}. \tag{16}$$

The forgetting factor $\lambda \in (0, 1]$ acts as the weight provided on the previous estimates obtained by RLS [26]–[28]. As $\lambda = 1$, more weight is placed on the older estimates, implying any changes in the system/measurement may not have an immediate impact to the SE. On the other hand, for $\lambda < 1$, the recent measurements/estimates have more weight and changes in the network impact the SE faster [28]–[30]. The measurement covariance matrix R_{se} is defined as

$$R_{\text{se}} = \text{diag}\big(n_v\mathcal{R}_v^T, n_w\mathcal{R}_w^T\big). \tag{17}$$

In the above equation, variables n_v and n_w are scalars while R_v and R_w are vectors containing the covariance of $y - C\hat{x}$ and $0_{(\text{rows}(T),1)} + T\hat{x}$, respectively. The steps involved in implementing the RLS algorithm are shown in Table I.

TABLE I
RLS ALGORITHM [27]

Model:	$\tilde{y}(k) = \tilde{C}(k)x(k) + v_{se}(k) \ \ v_{se}(k) \sim \mathcal{N}(0, \ R_{se}(k))$
Initialize:	$P_{se}(0) = E\left[(\hat{x}(0) - x)(\hat{x}(0) - x)^T\right]$ $x(0)^T = E\,[x]$
Gain:	$K_{se}(k) = P_{se}(k)\tilde{C}^T(k)\left[\tilde{C}(k)P_{se}^-(k)\tilde{C}^T(k) + \lambda R_{se}\right]^{-1}$
Update:	$P_{se}(k) = \frac{1}{\lambda}\,[P_{se}(k-1) - K_{se}(k)\tilde{C}(k)P_{se}(k-1)]$ $\hat{x}(k) = \hat{x}(k-1) + K_{se}(k)[y(k) - \tilde{C}(k)\hat{x}(k-1)]$

III. PARAMETER ESTIMATION

In this section, we present the AKF based PE algorithm through which we obtain real-time admittance estimation. The line admittances then help us to detect/identify a SAF on the microgrid.

A. Formulation of Admittance Equation for PE

As discussed in Section II, the estimate of microgrid's states comprising of nodal voltages $V(k) \in \mathbb{R}^N$, branch voltages $e(k) \in \mathbb{R}^E$ and line currents $l(k) \in \mathbb{R}^E$ are obtained by using the RLS algorithm and the measurement data. Since all of the line currents are estimated, an injection current vector can be obtained as

$$I(k) \ = \begin{pmatrix} I_1(k) & \cdots & I_N(k) \end{pmatrix}^T. \tag{18}$$

The nodal equation, consisting of admittance matrix $Y(k) \in \mathbb{R}^{N\times N}$ at time interval k, can then be derived as

$$I(k) = Y(k) \ V(k). \tag{19}$$

The admittance matrix $Y(k)$ contains the unknown elements to be estimated. We then transform the nodal equation (19) to linear regression form for AKF-based PE

$$\gamma\,(k) = \Phi(k) \ \Upsilon(k) + v_{\text{pe}}(k) \tag{20}$$

where $v_{\text{pe}}(k) \sim \mathcal{N}(0, R_{\text{pe}}(k))$ is the measurement noise, the output vector is defined by $\gamma\,(k)$, the line admittances are collected in $\Upsilon(k)$, and $\Phi(k)$ is a matrix obtained from (19) as follows [22]:

$$\begin{aligned} &\text{vec}(I\,(k)) = \text{vec}(Y(k)V(k)) \\ &\implies \underbrace{I(k)}_{\gamma\,(k)} = \underbrace{\big(V(k)^T \otimes \mathcal{I}_N\big)}_{\triangleq \Phi_Y(k)} \underbrace{\text{vec}(Y(k))}_{\Upsilon_Y(k)}. \end{aligned} \tag{21}$$

Since the admittance matrix $Y(k)$ is symmetric and can be considered a Laplacian (for a weighted graph of the dc microgrid without line to ground resistors [31]–[35]), it is possible to reduce the dimension of vector $\Upsilon_Y(k)$ to include only the lower triangular matrix elements of Y [as the diagonal elements can also be ignored (Laplacian property)]. Therefore, the number of parameters in this new vector is

$[([N][N-1])/2]$ which is a significant reduction in comparison to the earlier $N \times N$ elements.

For the following admittance matrix of size $N \times N$:

$$Y(k) = \begin{pmatrix} Y_{1,1}(k) & \cdots & Y_{1,N}(k) \\ \vdots & \ddots & \vdots \\ Y_{N,1}(k) & \cdots & Y_{N,N}(k) \end{pmatrix} \tag{22}$$

the vector consisting of the parameters being estimated is given by

$$\Upsilon_{\text{utop}}^T = \begin{pmatrix} Y_{2,1} & Y_{3,1} & \cdots & Y_{3,2} & Y_{4,2} & \cdots & Y_{N,N-1} \end{pmatrix}. \tag{23}$$

Since $\Upsilon_Y(k) = Q_Y \Upsilon_{\text{utop}}(k)$, for a proper matrix Q_Y, (21) can be simplified as

$$\gamma(k) = \left[\left(V(k)^T \otimes \mathcal{I}_N \right) Q_Y \right] \Upsilon_{\text{utop}}(k). \tag{24}$$

Finally, as the topology of a dc microgrid is known *a priori*, we can further reduce the vector containing the parameters to be estimated, to include only the lines that actually exist in the network. This is given by

$$\gamma(k) = \underbrace{\left[\left(V(k)^T \otimes \mathcal{I}_N \right) Q_Y M \right]}_{\Phi(k)} \Upsilon \tag{25}$$

where

$$\text{vec}(Y) = \Upsilon_Y = Q_Y \Upsilon_{\text{utop}} = Q_Y M \Upsilon \tag{26}$$

where Υ contains only the line admittances. Hence, over every iteration k, the line admittances are estimated through which a SAF can be detected.

B. AKF-Based PE

In this section, we present the implementation of AKF for PE. The line admittances estimated by AKF help in detecting/identifying a SAF on the microgrid. We begin by formulating the vector $\Upsilon(k)$ which consists of the parameters being estimated in a discrete linear system of the form

$$\Upsilon(k) = F(k-1)\Upsilon(k-1) + G(k-1)u(k-1) + w_{\text{pe}}(k-1). \tag{27}$$

The process noise is represented by vector $w_{\text{pe}}(k)$, and vector $u(k)$ is the input. However, for PE of line admittances, (27) is modified as

$$\Upsilon(k) = \Upsilon(k-1) + w_{\text{pe}}(k-1). \tag{28}$$

The estimate of $\Upsilon(k)$ at time k is given by $\hat{\Upsilon}(k)$. The covariance matrices using the above terms are defined as follows:

$$P_{\text{pe}}(k) \triangleq E\left[(\hat{\Upsilon}(k) - \Upsilon)(\hat{\Upsilon}(k) - \Upsilon)^T \right] \tag{29}$$

$$R_{\text{pe}}(k) \triangleq E\left[v_{\text{pe}}(k) v_{\text{pe}}(k)^T \right] \tag{30}$$

$$Q_{\text{pe}}(k) \triangleq E\left[w_{\text{pe}}(k) w_{\text{pe}}(k)^T \right]. \tag{31}$$

The error matrix P is initialized as follows:

$$P_{\text{pe}}(0) = E\left[(\hat{\Upsilon}(0) - \Upsilon)(\hat{\Upsilon}(0) - \Upsilon)^T \right]$$

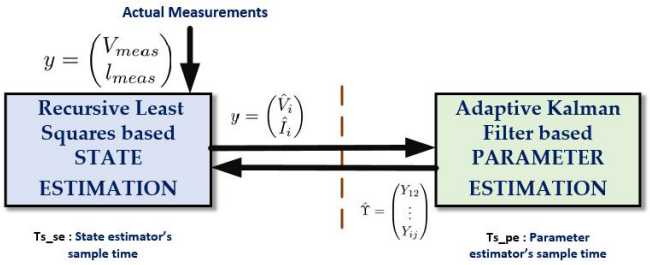

Fig. 1. Schematic of SE and PE.

which updates over each iteration. We typically fix the measurement and process noise covariance matrices in a KF [18]. However, for AKF only the measurement covariance matrix is fixed, $R_{\text{pe}} = n\,\mathcal{I}$ where n is positive gain. The gain of the AKF is given by

$$K_{\text{pe}}(k) = P_{\text{pe}}^-(k)\Phi^T(k)\left[\Phi(k) P_{\text{pe}}^-(k) \Phi^T(k) + R_{\text{pe}} \right]^{-1}. \tag{32}$$

The matrix $P_{\text{pe}}(k)^-$ denotes *a priori* error covariance estimate, and is computed as follows:

$$P_{\text{pe}}^-(k) = F(k-1)P_{\text{pe}}^+(k-1)F^T(k-1) + Q_{\text{pe}}(k-1) \tag{33}$$

$$\implies P_{\text{pe}}^-(k) = P_{\text{pe}}^+(k-1) + Q_{\text{pe}}(k-1). \tag{34}$$

Considering, Υ_i to be the ith element of Υ, the process noise covariance matrix denoted by $Q_{\text{pe}}(k)$ is evaluated at every step k as follows:

$$w_{\text{pe}_i} \triangleq \hat{\Upsilon}_i(k)^+ - \hat{\Upsilon}_i(k)^- \tag{35}$$

$$Q_{\text{pe}}(k) = \alpha\, \text{diag}\left[\left[w_{\text{pe}_1} \right]^2; \left[w_{\text{pe}_2} \right]^2; \left[w_{\text{pe}_3} \right]^2; \ldots \right]. \tag{36}$$

Variable α in the above equation is a positive gain. Similarly, the *a priori* parameter estimate is given by

$$\hat{\Upsilon}^-(k) = F(k-1)\hat{\Upsilon}^+(k-1) + G(k-1)u(k-1) \tag{37}$$

$$\Rightarrow \quad \hat{\Upsilon}^-(k) = \mathcal{I}\hat{\Upsilon}^+(k-1). \tag{38}$$

Finally, at time k, the optimal estimate is

$$P_{\text{pe}}^+(k) = P_{\text{pe}}^-(k) - K_{\text{pe}}(k)\Phi(k)P_{\text{pe}}^-(k) \tag{39}$$

$$\hat{\Upsilon}^+(k) = \hat{\Upsilon}^-(k) + K_{\text{pe}}(k)\left[y(k) - \Phi(k)\hat{\Upsilon}^-(k) \right]. \tag{40}$$

The steps involved in the implementation of AKF are summarized in Table II. Fig. 1 illustrates the SE–PE algorithm being implemented in this article. The fault detection and identification through the SE–PE technique is presented through a flowchart in Fig. 2.

IV. Case Study and Offline Simulation Results

In this section, we illustrate the ability of the proposed algorithm in estimation of line admittances, fault detection/identification, and robustness during nominal operating conditions of a dc microgrid.

TABLE II
AKF ALGORITHM [27]

Model:	$\Upsilon(k+1) = \mathcal{I}\Upsilon(k) + w_{pe}(k),$ $w_{pe}(k) \sim \mathcal{N}(0,\ Q_{pe}(k))$ $\gamma(k) = \Phi(k)\Upsilon(k) + v_{pe}(k),$ $v_{pe}(k) \sim \mathcal{N}(0,\ R_{pe}(k))$
Initialize:	$P_{pe}^{-}(0) = E\left[(\hat{\Upsilon}(0) - \Upsilon)(\hat{\Upsilon}(0) - \Upsilon)^T\right]$ $x(0)^T = E\ [\Upsilon]$
Gain:	$K_{pe}(k) = P_{pe}^{-}(k)\Phi^T(k)\left[\Phi(k)P_{pe}^{-}(k)\Phi^T(k) + R_{pe}\right]^{-1}$
Update:	$P_{pe}^{+}(k) = P_{pe}^{-}(k) - K_{pe}(k)\Phi(k)P_{pe}^{-}(k)$ $\hat{\Upsilon}^{+}(k) = \hat{\Upsilon}^{-}(k) + K_{pe}(k)\left[\gamma(k) - \Phi(k)\hat{\Upsilon}^{-}(k)\right]$
Propagation:	$w_{pe_i} \triangleq \hat{\Upsilon}_i(k)^{+} - \hat{\Upsilon}_i(k)^{-}$ $Q_{pe}(k) = \alpha\ \text{diag}\left[\left[w_{pe_1}\right]^2; \left[w_{pe_2}\right]^2; \left[w_{pe_3}\right]^2; \cdots\right]$ $P_{pe}^{-}(k) = P_{pe}^{+}(k-1) + Q_{pe}(k-1)$ $\hat{\Upsilon}^{-}(k+1) = \hat{\Upsilon}^{+}(k)$

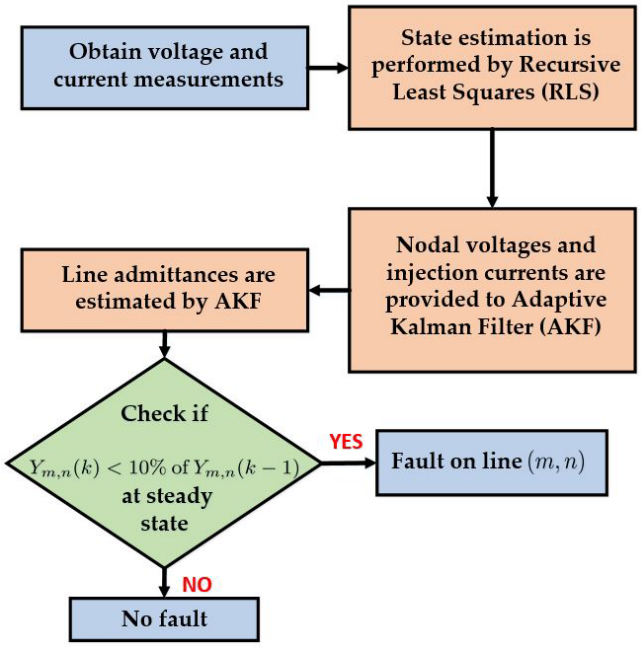

Fig. 2. Flowchart of fault detection and identification.

A. Microgrid Model

The seven node dc microgrid shown in Fig. 3 will be used for the simulation results. The network can be defined as a graph $\mathcal{G} = (\bar{\mathcal{V}}, \mathcal{E})$, where $\bar{\mathcal{V}} = \{0, 1, 2, \ldots, 7\}$, $\mathcal{E} = \{(1, 0_g), \ldots, (6, 7)\}$, and it includes five generators, three CPLs. The reduced set of nodes is given by $\mathcal{V} = \{1, 2, \ldots, 7\}$. The microgrid is varied over three cases consisting of different number of sensors and their placement, as shown in Fig. 3.

TABLE III
DC MICROGRID SIMULATION PARAMETERS

Line	Length (miles)	Inductance (H)	Resistance (Ω)	Admittance (Ω^{-1})
(1,3)	0.1	1.6e-4	0.12	8.33
(2,4)	0.1	1.6e-4	0.12	8.33
(3,6)	0.125	2e-4	0.15	6.67
(4,7)	0.125	2e-4	0.15	6.67
(5,6)	0.15	2.4e-4	0.18	5.55
(6,7)	0.05	8e-5	0.06	16.67

The placement of sensors is typically decided by the application. However, there are approaches to find an optimal sensor placement [36]–[38] in a microgrid. Assuming that a total of p sensors (voltage and current) are to be used/deployed, the total number of sensor placements possible is given by

$$\mathcal{O}_{C_p} = \binom{\mathcal{O}}{p} = \frac{\mathcal{O}!}{(\mathcal{O}-p)!(p)!} \tag{41}$$

where $\mathcal{O} = N + E$, N is the number of nodes in the network at which a voltage sensor can be placed and E is the number of edges/lines in the network where a current sensor can be placed. For the three cases shown in Fig. 3, we chose $p = 16, 14, 13$, respectively.

The simulation was conducted using MATLAB Simpower Systems for 1 s with a simulation time step of 5 μs. Each generator and load is connected to the network through a buck converter. The inductance and capacitance of each converter are 1 mH and 1 mF, respectively. The nominal dc voltage of the network is assumed to be 390 V. The input voltage of the generator converters is 600 V. The generators share power through traditional droop control [39]. The network includes five sources at nodes 1, 2, 4, 5, 7 and three loads at nodes 3, 4, 6. The initial value of the load currents at nodes 3, 4, and 6 are 175, 150, and 125 A, respectively, with an output load side voltage of 220 V. The total power consumed by the loads is 100 kW.

The resistance and inductance values for each line are shown in Table III. After a SAF occurs, the line $(3, 6)$ shows an increase in resistance from 0.15 Ω to 1.65 Ω. Similarly, line $(6, 7)$ increases its resistance from 0.06 Ω to 0.66 Ω and line $(5, 6)$ increases its resistance from 0.18 Ω to 1.98 Ω. The SAF model considered in this article is then composed of a series resistance, whose value can be computed from a classical nonlinear arc model (e.g., Paukert equation [40], heuristic equations [41], etc.), evaluated at the nominal network voltage (390 V) and steady-state line current [42]. This model helps simplify the arc (slower time scale) for the faster time step and scale used in simulation.

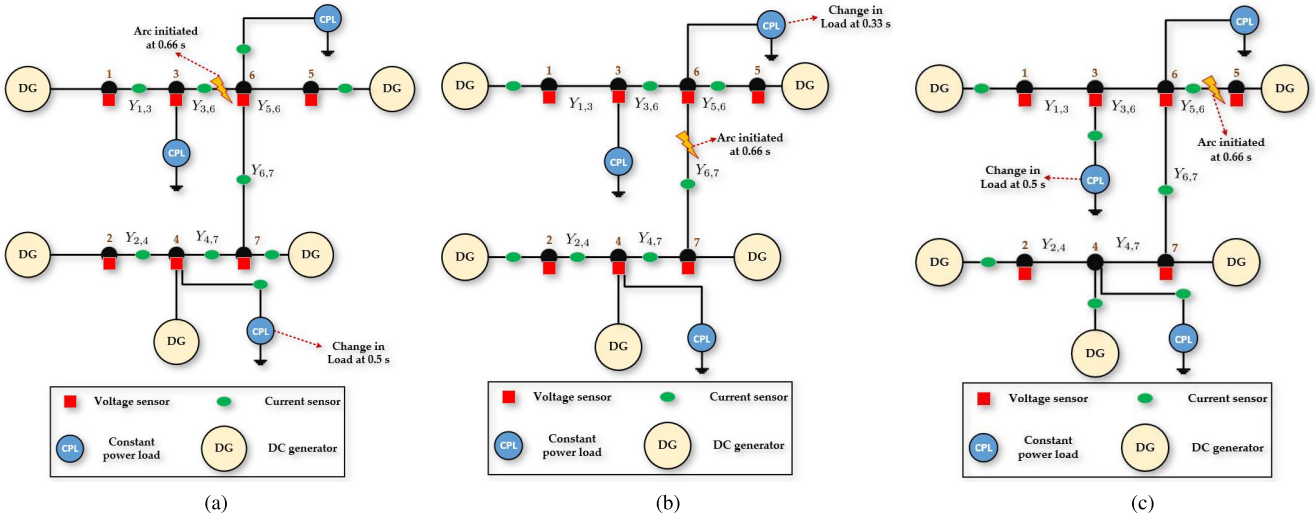

Fig. 3. Simulation results: placement of voltage and line current measuring sensors for the seven node dc microgrid. (a) Case 1: Placement of sensors over the microgrid. Sensors used: 16. (b) Case 2: Placement of sensors over the microgrid. Sensors used: 14. (c) Case 3: Placement of sensors over the microgrid. Sensors used: 13.

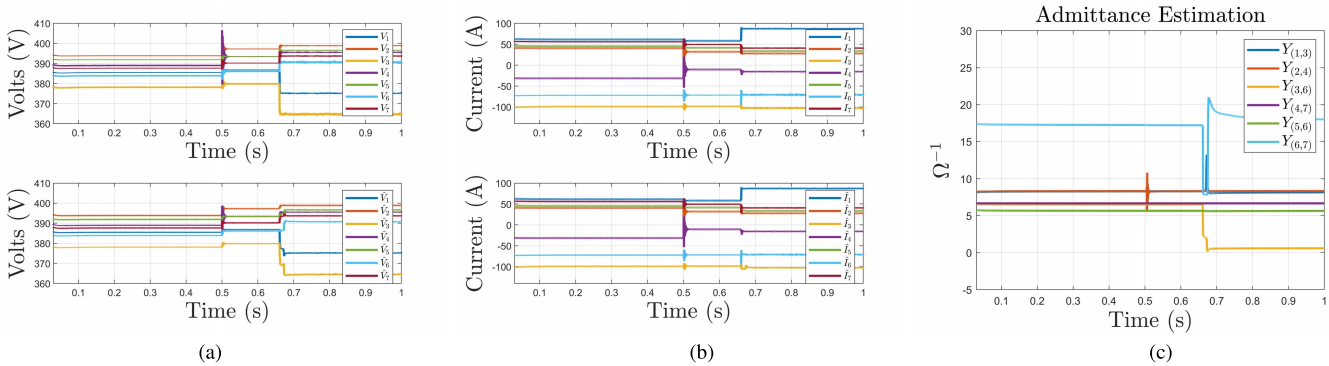

Fig. 4. Case 1: Simulation result when there is a change in current by load 4 at $t = 0.5$ s, followed by a series arc at $t = 0.66$ s on line $(3, 6)$. (a) Plot of actual nodal voltages (top). Estimated nodal voltages (bottom). (b) Plot of actual injection currents (top). Estimated injection currents (bottom). (c) Plot of line admittances showing fault detection.

In terms of line admittance, a SAF on a line causes its admittance value to drop. Three cases are considered as follows.

1) *Case 1:* Change in load 4 at $t = 0.5$ s, followed by a SAF on line $(3, 6)$ at $t = 0.66$ s.
2) *Case 2:* Change in load 6 at $t = 0.33$ s, followed by a SAF on line $(6, 7)$ at $t = 0.66$ s.
3) *Case 3:* Change in load 3 at $t = 0.5$ s, followed by a SAF on line $(5, 6)$ at $t = 0.66$ s.

B. Case 1

A microgrid with 16 sensors shown in Fig. 3(a) is simulated for SAF detection and identification on line (3, 6). The estimation of nodal voltages and nodal current injections are shown in Fig. 4(a) and (b), respectively. To attest the fact that change in load currents (nominal dc operations) do not affect the admittance estimation, we induce a change at the load side of the buck converter placed at node 4 by reducing its current from 150 to 90 A at $t = 0.5$ s, as shown in Fig. 4(b). The admittance shows minimal fluctuations during the change of current as seen in Fig. 4(c). Finally, a SAF was triggered on line (3, 6) at $t = 0.66$ s which is successfully detected, as the yellow line showing the admittance value decreases.

In Fig. 4(c), the line admittance estimation of (6, 7) shows a transient when the SAF is triggered on line (3, 6) at $t = 0.66$ s. However, this transient does not affect the line admittance estimation in long term as the admittance value of (6, 7) eventually settles to its original value. For SAF detection, we are interested in the steady-state value (true admittance) which is attained after such transient stages. To confirm a SAF, a larger difference in the steady-state value of the line admittance is needed, as shown in Fig. 2. Furthermore, a window can be implemented that checks the change in line admittance with the original pre-fault line admittance. If the estimated line admittance value remains lower than the original line admittance over consecutive windows, we can deduce a SAF occurrence on that particular line.

C. Case 2

In this case, we test the SAF detection on line (6, 7) while using 14 sensors as shown in Fig. 3(b). Fig. 5(a) and (b) show the estimation of nodal voltages and nodal current injections respectively by RLS. At time $t = 0.33$ s, the load at node 6

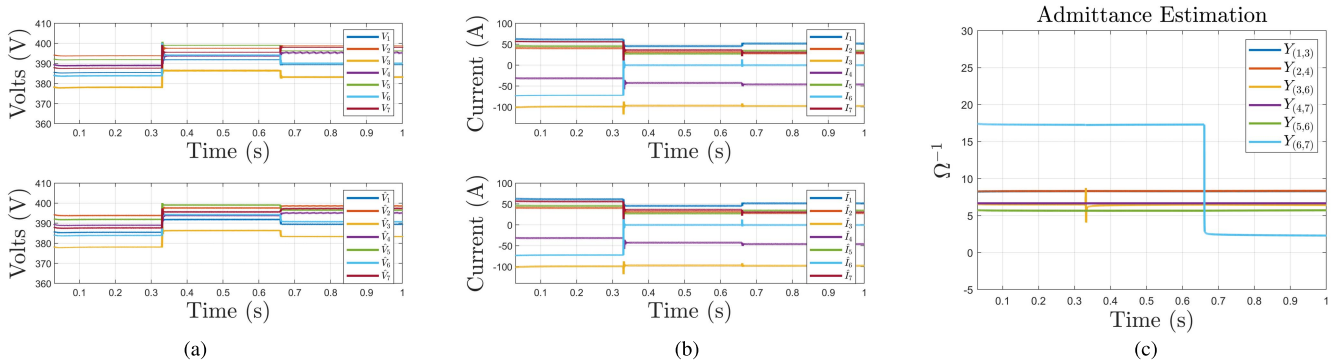

Fig. 5. Case 2: Simulation result when there is a change in current by Load 6 at $t = 0.33$ s, followed by a series arc at $t = 0.66$ s on line $(6, 7)$. (a) Plot of actual nodal voltages (top). Estimated nodal voltages (bottom). (b) Plot of actual injection currents (top). Estimated injection currents (bottom). (c) Plot of line admittances showing fault detection.

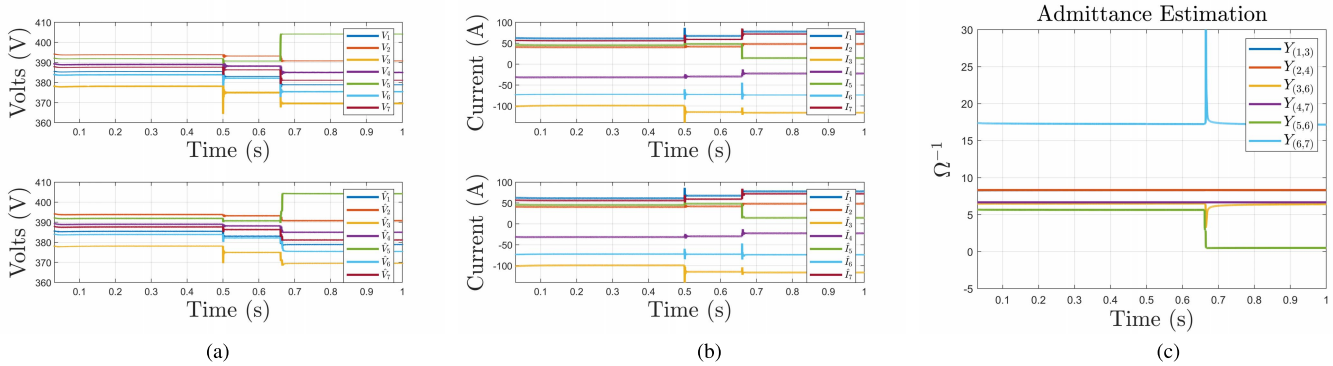

Fig. 6. Case 3: Simulation result when there is a change in current by Load 3 at $t = 0.05$ s, followed by a series arc at $t = 0.66$ s on line $(5, 6)$. (a) Plot of actual nodal voltages (top). Estimated nodal voltages (bottom). (b) Plot of actual injection currents (top). Estimated injection currents (bottom). (c) Plot of line admittances showing fault detection.

stops drawing current, as shown in Fig. 5(b). However, as seen in Fig. 5(c), the line admittance estimation shows very little disturbance caused by the load change. Furthermore, the SAF on line (6, 7) was successfully detected and identified at time $t = 0.66$ s as seen in Fig. 5(c), where the light blue colored line shows a drop in the admittance value.

D. Case 3

In this case, we test the SAF detection on line $(5, 6)$ while using 13 sensors as shown in Fig. 3(c). Fig. 6(a) and (b) show the estimation of nodal voltages and nodal current injections respectively by RLS. At time $t = 0.5$ s, the current drawn at the load side of the buck converter at node 3 is increased from 175 to 205 A, as shown in Fig. 6(b). However, as seen in Fig. 6(c) the line admittance estimation shows very little disturbance caused by the load change. Furthermore, the SAF on line (5, 6) was successfully detected and identified at time $t = 0.66$ s as seen in Fig. 6(c), where the green colored line shows a drop in the admittance value.

Finally, we would like to state that the RLS- and AKF-based SE–PE are slightly affected by disturbances such as load changes and other common dc microgrid operation. In general, these disturbances do not cause a significant change in the steady-state value of the estimates, but rather introduce transients (RLS/AKF estimates) for a very short duration of time. Afterward, the line admittance estimates settle to their actual values. When considering a SAF, the line admittance changes to a lower value caused by the additional resistance added by the SAF. Hence, unlike the load changes in the dc microgrid, a SAF fundamentally reduces the steady state value of the line admittance after the transient stage.

V. Control Hardware in Loop Results

The microgrid shown in Fig. 3 was built using 16 measurement sensors on the PLECS RT Box [43]. The model is simulated at a time step of 10 μs. Due to the timing constraints, buck converters on the load side were excluded and the line inductances were lowered to $1/10^{th}$ of their values used in simulation results (see Table III). The OP-4510 from OPAL RT [44] obtains the measurements from PLECS RT Box at a time step of 100 μs. The RLS built in OP-4510 estimates the states e, V, l, using (11) and (12). The estimate of nodal voltages and injection currents obtained from the SE is provided to the AKF. The AKF then uses (25) written in the format shown in (20) for estimating the parameters (line admittances). The real-time interaction of the PLECS and OPAL RT boxes is shown in Fig. 7(a) while the hardware setup consisting of the two RT boxes, oscilloscope, and the computer can be seen in Fig. 7(b). The estimation of admittances on lines $(2, 4)$, $(3, 6)$, $(5, 6)$, and $(4, 7)$ is shown in Fig. 8. A load current change from 150 to 90 A at node 4 shows no disturbance in the line admittance estimation while the SAF on line $(3, 6)$ is detected and identified.

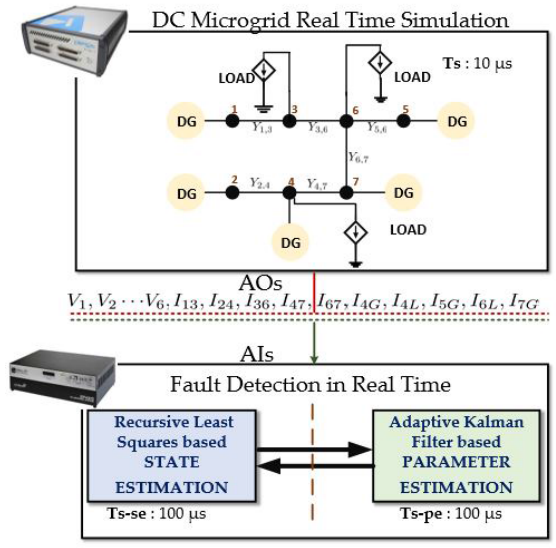

(a)

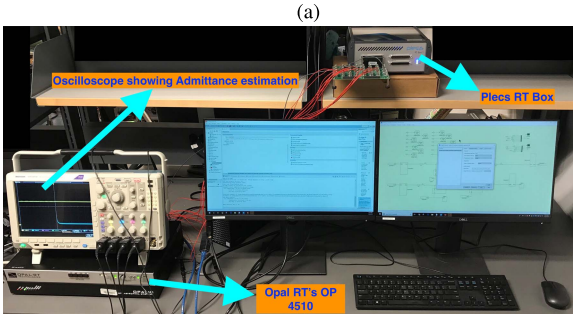

(b)

Fig. 7. CHIL results of series arc in line $Y_{(3,6)}$ and admittance estimation. (a) Real-time interaction of Plecs RT and Opal RT. (b) Overview of the CHIL setup.

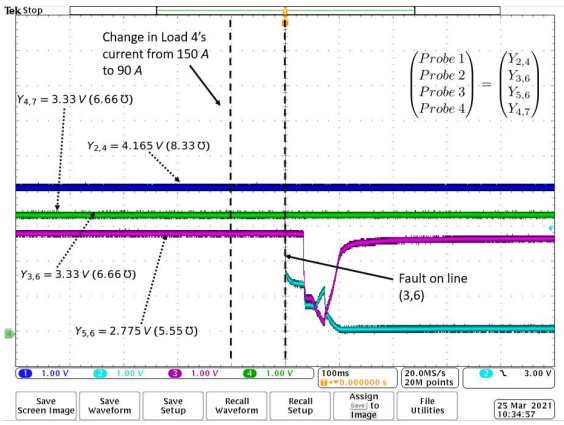

Fig. 8. CHIL: line admittance estimation showing SAF detection on line (3, 6).

VI. Experimental Results

In this section, we present the experimental results through which we can analyze the potential of the RLS-KF-based SE–PE for SAF detection and faulted line identification on a four node dc microgrid test-bed.

A. Test-Bed Description

The four node test-bed includes one generator connected at node 1 and two CPLs connected at nodes 3 and 4, respectively. The generator at node 1 is a 20 kW Magna PS [45]. The

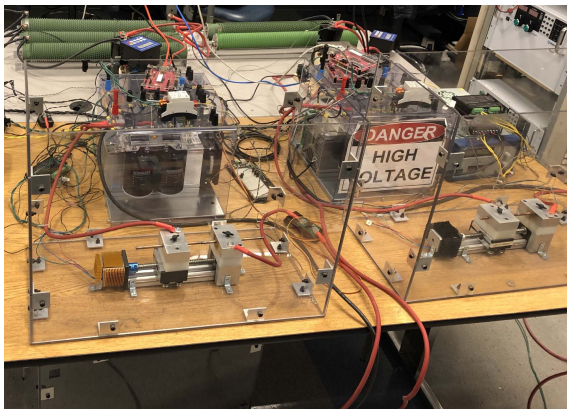

Fig. 9. Hardware setup for experimental results.

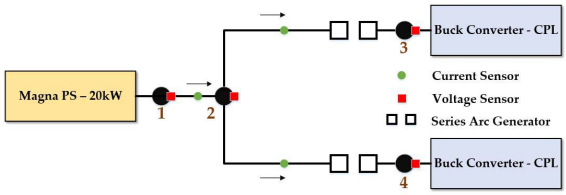

(a)

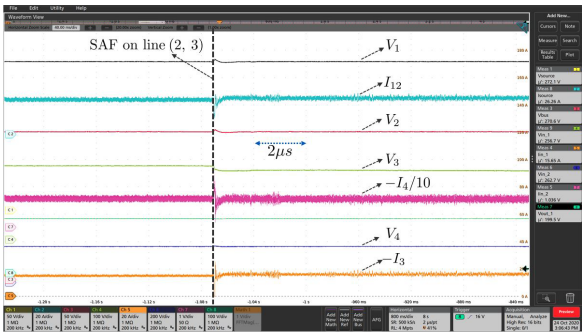

(b)

Fig. 10. Experimental results: sensor placement and the oscilloscope plots. (a) Sensor placement on the four node dc microgrid. (b) Measurements on oscilloscope.

input voltage from the generator is 270 V. The bus voltage is measured at node 2 which acts as an internal node. The power flow from node 2 then splits to loads at nodes 3 and 4. The load at node 3 draws a current of 15 A and the load at node 4 draws a current of 10 A. The CPLs are based on closed loop-controlled buck converters (shown in Fig. 9) from Semikron [46]. The 10 mH inductors were purchased from Hammond Manufacturing [47], and the capacitors rated at 750 V from Cornell Dubilier Electronics (CDE) [48]. The sensor placement and the dc microgrid topology is presented in Fig. 10(a). The real-time data obtained through the oscilloscope are shown in Fig. 10(b).

B. Results

For experimental testing of the SE–PE technique, the SAF was set to trigger on line (2, 3) at time $t = 2.29$ s on the dc microgrid shown in Fig. 9. The nodal voltages and current injections, shown in Fig. 11(a) and (b), are obtained from the SE performed by the RLS algorithm. The line admittance estimation by AKF is shown in Fig. 12 from which we can

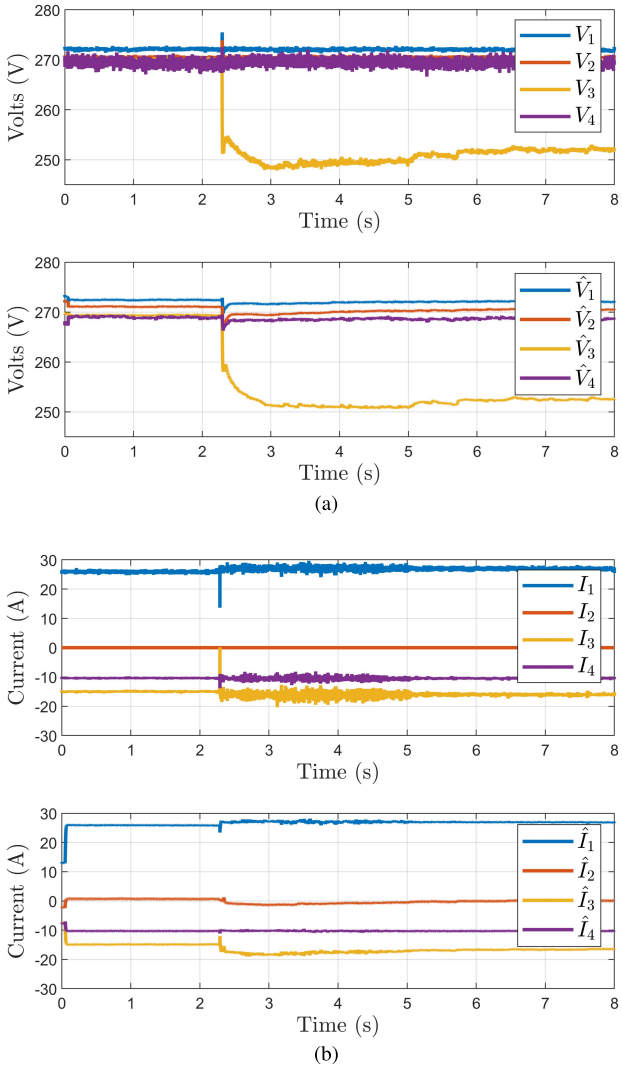

Fig. 11. Experimental results for SE by RLS. (a) Plot of actual nodal voltages (top). Estimated nodal voltages (bottom). (b) Plot of actual injection currents (top). Estimated injection currents (bottom).

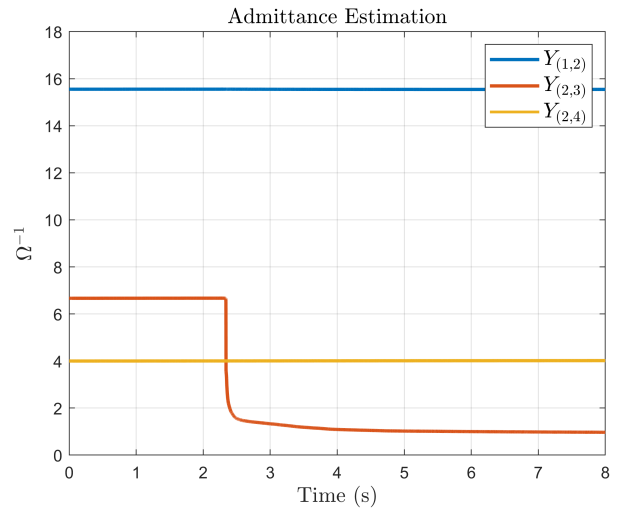

Fig. 12. Line admittance estimation showing fault detection on line (2, 3).

easily conclude that the red line showing a significant drop in the admittance value is the faulted line. The experimental result shows that the SAF on line (2, 3) was successfully detected and identified by the proposed SE–PE approach.

VII. Conclusion and Future Work

This article presents a RLS and AKF-based SE and PE for SAF detection and faulted line identification on a dc microgrid. The RLS state estimator uses measurement data and the STA to provide the AKF with the estimates of nodal voltages and injection currents. The AKF parameter estimator uses nodal voltages and injection currents to estimate admittances of the lines across the microgrid. The SE and PE technique's performance was evaluated through simulation, CHIL, and hardware-based experimental setup. The results show a quick and successful detection/identification of a SAF on a dc microgrid. Furthermore, the objective of the article is to detect and identify the SAF affected line as early as possible and is optimized to satisfy this criterion. The results presented in this article show SAF detection and the identification of the faulted line within 10 ms while measurements are obtained at 0.1 ms.

In future, we will improve the SE and PE to detect faulty sensors and cyber-attacks. Furthermore, SE and PE will be verified using least possible number of sensors, while still maintaining full observability of every line in the microgrid which will require optimal sensor placement strategy.

References

[1] T. Dragicevic, J. C. Vasquez, J. M. Guerrero, and D. Skrlec, "Advanced LVDC electrical power architectures and microgrids: A step toward a new generation of power distribution networks," *IEEE Electrific. Mag.*, vol. 2, no. 1, pp. 54–65, Mar. 2014.

[2] L. E. Zubieta, "Are microgrids the future of energy?: DC microgrids from concept to demonstration to deployment," *IEEE Electrific. Mag.*, vol. 4, no. 2, pp. 37–44, Jun. 2016.

[3] X. Yao, L. Herrera, and J. Wang, "Impact evaluation of series DC arc faults in DC microgrids," in *Proc. IEEE Appl. Power Electron. Conf. Expo. (APEC)*, Mar. 2015, pp. 2953–2958.

[4] X. Yao, "Study on DC arc faults in ring-bus DC microgrids with constant power loads," in *Proc. IEEE Energy Convers. Congr. Expo. (ECCE)*, Sep. 2016, pp. 1–5.

[5] X. Yao, L. Herrera, L. Yue, and H. Cai, "Experimental study of series DC arc in distribution systems," in *Proc. IEEE Energy Convers. Congr. Expo. (ECCE)*, Sep. 2018, pp. 1–5.

[6] Q. Xiong *et al.*, "Series arc fault detection and localization in DC distribution system," *IEEE Trans. Instrum. Meas.*, vol. 69, no. 1, pp. 122–134, Jan. 2020.

[7] J.-C. Gu, D.-S. Lai, J.-M. Wang, J.-J. Huang, and M.-T. Yang, "Design of a DC series arc fault detector for photovoltaic system protection," *IEEE Trans. Ind. Appl.*, vol. 55, no. 3, pp. 2464–2471, May 2019.

[8] Z. Wang and R. S. Balog, "Arc fault and flash signal analysis in DC distribution systems using wavelet transformation," *IEEE Trans. Smart Grid*, vol. 6, no. 4, pp. 1955–1963, Jul. 2015.

[9] A. Shekhar, L. Ramírez-Elizondo, S. Bandyopadhyay, L. Mackay, and P. Bauera, "Detection of series arcs using load side voltage drop for protection of low voltage DC systems," *IEEE Trans. Smart Grid*, vol. 9, no. 6, pp. 6288–6297, Nov. 2018.

[10] L. Herrera and X. Yao, "Parameter identification approach to series DC arc fault detection and localization," in *Proc. IEEE Energy Convers. Congr. Expo. (ECCE)*, Sep. 2018, pp. 497–501.

[11] K. K. Gajula, L. Herrera, and X. Yao, "Detection of series DC arc on a distribution node using discrete-time parameter identification techniques," in *Proc. IEEE Appl. Power Electron. Conf. Expo. (APEC)*, Mar. 2019, pp. 3007–3012.

[12] K. Gajula and L. Herrera, "Detection and localization of series arc faults in DC microgrids using Kalman filter," *IEEE J. Emerg. Sel. Topics Power Electron.*, vol. 9, no. 3, pp. 2589–2596, Jun. 2021.

[13] Q. Lu, Z. Ye, M. Su, Y. Li, Y. Sun, and H. Huang, "A DC series arc fault detection method using line current and supply voltage," *IEEE Access*, vol. 8, pp. 10134–10146, 2020.

[14] M. Kavi, Y. Mishra, and M. Vilathgamuwa, "DC arc fault detection for grid-connected large-scale photovoltaic systems," *IEEE J. Photovolt.*, vol. 10, no. 5, pp. 1489–1502, Sep. 2020.
[15] V. Le, X. Yao, C. Miller, and B.-H. Tsao, "Series DC arc fault detection based on ensemble machine learning," *IEEE Trans. Power Electron.*, vol. 35, no. 8, pp. 7826–7839, Aug. 2020.
[16] V. Le and X. Yao, "Ensemble machine learning based adaptive arc fault detection for DC distribution systems," in *Proc. IEEE Appl. Power Electron. Conf. Expo. (APEC)*, Mar. 2019, pp. 1984–1989.
[17] S. Lu, T. Sirojan, B. T. Phung, D. Zhang, and E. Ambikairajah, "DA-DCGAN: An effective methodology for DC series arc fault diagnosis in photovoltaic systems," *IEEE Access*, vol. 7, pp. 45831–45840, 2019.
[18] K. Gajula, X. Yao, and L. Herrera, "Dual state–parameter estimation for series arc fault detection on a DC microgrid," in *Proc. IEEE Energy Convers. Congr. Expo. (ECCE)*, Oct. 2020, pp. 4649–4655.
[19] J. Zhang, Y. Wang, Y. Weng, and N. Zhang, "Topology identification and line parameter estimation for non-PMU distribution network: A numerical method," *IEEE Trans. Smart Grid*, vol. 11, no. 5, pp. 4440–4453, Sep. 2020.
[20] J. Yu, Y. Weng, and R. Rajagopal, "PaToPa: A data-driven parameter and topology joint estimation framework in distribution grids," *IEEE Trans. Power Syst.*, vol. 33, no. 4, pp. 4335–4347, Jul. 2018.
[21] S. Grotas, Y. Yakoby, I. Gera, and T. Routtenberg, "Power systems topology and state estimation by graph blind source separation," *IEEE Trans. Signal Process.*, vol. 67, no. 8, pp. 2036–2051, Apr. 2019.
[22] O. Ardakanian *et al.*, "On identification of distribution grids," *IEEE Trans. Control Netw. Syst.*, vol. 6, no. 3, pp. 950–960, Sep. 2019.
[23] D. Gorinevsky, S. Boyd, and S. Poll, "Estimation of faults in DC electrical power system," in *Proc. Amer. Control Conf.*, 2009, pp. 4334–4339.
[24] L. O. Chua, C. A. Desoer, and E. S. Kuh, *Linear and Nonlinear Circuits*. New York, NY, USA: McGraw-Hill, 1987.
[25] B. Park, J. Netha, M. C. Ferris, and C. L. DeMarco, "Sparse tableau approach for power system analysis and design," in *Proc. North Amer. Power Symp. (NAPS)*, Sep. 2018, pp. 1–6.
[26] D. Simon, *Optimal State Estimation: Kalman, H Infinity, and Nonlinear Approaches*. Hoboken, NJ, USA: Wiley, 2006.
[27] J. L. Crassidis and J. L. Junkins, *Optimal Estimation of Dynamic Systems*. London, U.K.: Chapman & Hall, 2011.
[28] M. Ahmeid, M. Armstrong, S. Gadoue, M. Al-Greer, and P. Missailidis, "Real-time parameter estimation of DC–DC converters using a self-tuned Kalman filter," *IEEE Trans. Power Electron.*, vol. 32, no. 7, pp. 5666–5674, Jul. 2017.
[29] C. Paleologu, J. Benesty, and S. Ciochina, "A robust variable forgetting factor recursive least-squares algorithm for system identification," *IEEE Signal Process. Lett.*, vol. 15, pp. 597–600, Oct. 2008.
[30] A. Vahidi, A. Stefanopoulou, and H. Peng, "Recursive least squares with forgetting for online estimation of vehicle mass and road grade: Theory and experiments," *Vehicle Syst. Dyn.*, vol. 43, no. 1, pp. 31–55, 2005.
[31] T. Ding, R. Bo, Y. Yang, and F. Blaabjerg, "Impact of negative reactance on definiteness of B-matrix and feasibility of DC power flow," *IEEE Trans. Smart Grid*, vol. 10, no. 2, pp. 1725–1734, Mar. 2019.
[32] F. Dörfler and F. Bullo, "Spectral analysis of synchronization in a lossless structure-preserving power network model," in *Proc. 1st IEEE Int. Conf. Smart Grid Commun.*, Oct. 2010, pp. 179–184.
[33] X. Li, H. V. Poor, and A. Scaglione, "Blind topology identification for power systems," in *Proc. IEEE Int. Conf. Smart Grid Commun. (SmartGridComm)*, Oct. 2013, pp. 91–96.
[34] E. W. Weisstein. (1999). *Laplacian Matrix*. [Online]. Available: https://mathworld.wolfram.com/
[35] F. Dorfler and F. Bullo, "Synchronization of power networks: Network reduction and effective resistance," *IFAC Proc. Volumes*, vol. 43, no. 19, pp. 197–202, 2010.
[36] J. Dong *et al.*, "Two-stage state estimation algorithm for distribution network analysis," in *Proc. Australas. Univ. Power Eng. Conf. (AUPEC)*, Nov. 2018, pp. 1–6.
[37] M. Uddin, A. Kuh, A. Kavcic, and T. Tanaka, "Approximate solutions and performance bounds for the sensor placement problem," in *Proc. IEEE 3rd Int. Conf. Smart Grid Commun. (SmartGridComm)*, Nov. 2012, pp. 31–36.
[38] S. Martínez and F. Bullo, "Optimal sensor placement and motion coordination for target tracking," *Automatica*, vol. 42, no. 4, pp. 661–668, Apr. 2006.
[39] J. M. Guerrero, J. C. Vasquez, J. Matas, L. G. de Vicuna, and M. Castilla, "Hierarchical control of droop-controlled AC and DC microgrids—A general approach toward standardization," *IEEE Trans. Ind. Electron.*, vol. 58, no. 1, pp. 158–172, Jan. 2011.
[40] X. Yao, L. Herrera, S. Ji, K. Zou, and J. Wang, "Characteristic study and time-domain discrete-wavelet-transform based hybrid detection of series DC arc faults," *IEEE Trans. Power Electron.*, vol. 29, no. 6, pp. 3103–3115, Jun. 2014.
[41] F. M. Uriarte *et al.*, "A DC arc model for series faults in low voltage microgrids," *IEEE Trans. Smart Grid*, vol. 3, no. 4, pp. 2063–2070, Dec. 2012.
[42] X. Yao, "Study on DC arc faults in ring-bus DC microgrids with constant power loads," in *Proc. IEEE Energy Convers. Congr. Expo. (ECCE)*, Sep. 2016, pp. 1–5.
[43] *Plexim—Lectrical Engineering Software*. Accessed: Nov. 1, 2021. [Online]. Available: https://www.plexim.com/products/rt_box
[44] *Opal-RT Technologies*. Accessed: Nov. 1, 2021. [Online]. Available: https://www.opal-rt.com
[45] *Magna Power Supplies*. Accessed: Nov. 1, 2021. [Online]. Available: https://magna-power.com/products/magnadc/ts
[46] *Semiteach IGBT Module Stack*. Accessed: Nov. 1, 2021. [Online]. Available: https://www.semikron-shop.com/en/stacks/semiteach/semiteach-b6u-e1cif-b6ci.html
[47] *Inductors*. Accessed: Nov. 1, 2021. [Online]. Available: https://www.hammfg.com/electronics/transformers/choke/153-159
[48] *Capacitors*. Accessed: Nov. 1, 2021. [Online]. Available: https://www.cde.com/capacitors

Kaushik Gajula (Graduate Student Member, IEEE) received the B.E. degree in electronics and communication engineering from SRM University, Chennai, India, in 2016, and the M.S. degree in electrical engineering from the Rochester Institute of Technology (RIT), Rochester, NY, USA, in 2018. He is currently pursuing the Ph.D. degree in electrical engineering with the University at Buffalo (SUNY), Buffalo, NY, USA.

His research interests include modeling, control and optimization of dc microgrids, fault detection and parameter/state estimation by optimal estimation methods, and control hardware in the loop validation.

Lalit Kishore Marepalli (Graduate Student Member, IEEE) received the B.E. degree in electrical engineering from Jawaharlal Nehru Technological University (JNTU), Hyderabad, India, in 2014, and the M.S. degree in electrical engineering from New York University, New York, NY, USA, in 2016. He is currently pursuing the Ph.D. degree in electrical engineering with the University at Buffalo (SUNY), Buffalo, NY, USA.

His current research interests include modeling, control and optimization of dc microgrids, optimal power flow, and control hardware in the loop validation.

Xiu Yao (Member, IEEE) received the B.Sc. and M.Sc. degrees in electrical engineering from Xi'an Jiaotong University, Xi'an, China, in 2007 and 2010, respectively, and the Ph.D. degree from The Ohio State University, Columbus, OH, USA, in 2015.

She is currently an Assistant Professor with the Department of Electrical Engineering, University at Buffalo, Buffalo, NY, USA. Her research interests include dc arc detection, dc microgrid protection and control, and high voltage dc transmission.

Luis Herrera (Member, IEEE) received the B.S. degree in electrical engineering from The University of Tennessee at Martin, Martin, TN, USA, in 2010, and the Ph.D. degree in electrical engineering from The Ohio State University, Columbus, OH, USA, in 2015.

From 2015 to 2016, he was a Research Engineer with the Advanced Power Components Group, University of Dayton Research Institute, Dayton, OH, USA. He was also an Assistant Professor with the Rochester Institute of Technology, Rochester, NY, USA, from 2016 to 2018. He is currently an Assistant Professor with the Department of Electrical Engineering, University at Buffalo, Buffalo, NY, USA. His research interests include modeling and control of power electronic systems, dc microgrids, fault detection using parameter estimation techniques, and optimal utilization of energy sources.